COMPUTATIONAL MODELLING ENABLES ROBUST MULTIDIMENSIONAL NANOSCOPY

MATTHEW D. LEW

Department of Electrical and Systems Engineering,
Washington University in St. Louis, MO 63130, USA

Present State of Computational Modelling in Fluorescence Nanoscopy

Computation is inescapable in modern fluorescence nanoscopy, ranging from simple tasks such as counting photons (and simple manipulations thereof, e.g., in RESOLFT [1] and MINFLUX [2]) to fusing together multiple images taken under different conditions (e.g., in SIM [3] and ISM [4]) to repeatedly localizing single fluorescent molecules [5, 6] using a model PSF (as in single-molecule localization microscopy [SMLM], (F)PALM, STORM, and PAINT). However, the power of computational imaging lies in its ability to transcend the centuries-old paradigm of point-to-point mapping from object to camera [7] common in traditional microscopy; explicitly integrating computation and physical optics together enables new capabilities that cannot be realized by conventional techniques alone. Further, computational modelling also allows experimenters to optimize and rigorously validate any proposed technology before setting foot in the lab.

Classical Fisher information theory has been used to characterize [8–13] and design [14–17] multidimensional nanoscopes since they were first demonstrated. The power of computing Fisher information lies in its ability to bound the best-possible variance of any unbiased estimator, called the Cramér Rao bound (CRB) [18]. Therefore, independent of the computational algorithm used to generate super-resolved images, Fisher information can be used to compare the performance of any variant of fluorescence nanoscopy. Another advantage is the quantitative specificity of this metric; unlike many other (loose) statistical bounds [19], the CRB can be optimized computationally to design the best-possible optical system for a certain imaging task. Such analyses show that the tetrapod family [16, 20] of point spread functions (PSFs) achieves higher localization precision in 3D SMLM than other approaches [17].

The classical model-based approach for designing optical nanoscopes involves choosing (1) the appropriate forward model for a given imaging task (e.g., localizing an isolated fluorescent emitter in 3D space), (2) the desired performance metric

to evaluate a proposed design (e.g., CRB with Poisson shot noise), and (3) the methodology to achieve the best-possible performance (e.g., a gradient decent algorithm with certain constraints). However, it is difficult to maximize both emitter detectability, which requires a PSF to be compact on the camera, and measurement precision, which requires the PSF to change significantly with the parameter of interest, e.g., z-position, dipole orientation, or emission wavelength. However, recent deep learning methods promise to overcome these challenges. Neural networks have been proposed to replace traditional optimization algorithms for axial localization and colour identification in standard microscopes without colour filters [21]. Further, neural networks can be used to design optical nanoscopes that maximize colour classification accuracy, again without the use of traditional filters [22].

Recent Contributions to Computational Modelling in Fluorescence Nanoscopy

My lab is developing new technologies to augment standard SMLM with new capabilities, such as long-term imaging of amyloid fibrils [26]. Another example is the Tri-spot PSF [23, 24], which measures all degrees of freedom related to the orientational dynamics of SMs without angular degeneracy. A key insight of our analysis is that the orientational dynamics of any dipole emitter may be parameterized in terms of six orientational second moments, $\mathbf{M} = [\langle\mu_x^2\rangle, \langle\mu_y^2\rangle, \langle\mu_z^2\rangle, \langle\mu_x\mu_y\rangle, \langle\mu_x\mu_z\rangle, \langle\mu_y\mu_z\rangle]$, which are a function of a dipole's orientation $\mu = [\mu_x, \mu_y, \mu_z]$ averaged over a single measurement (i.e., a camera frame). (This orientation vector μ may also be expressed in spherical coordinates using a polar angle θ and azimuthal angle φ.) Therefore, to measure the brightness and orientational dynamics of an SM, a PSF must have at minimum six degrees of freedom to measure these parameters. It follows that designing a PSF to contain six discrete spots would enable scientists to measure all possible orientational dynamics without degeneracy, while also maximizing detectability, even for weak SMs. Thus, we designed a three-sector linear phase mask to create the Tri-spot PSF within a modified polarized fluorescence microscope. The Tri-spot PSF reveals depolarization within fluorescent beads that is difficult to detect using other methods, and it can also be used to observe rotational dynamics of fluorophores within polymer thin films that are not observable by conventional SMLM (Figs. 1(a)–1(d)). It achieves an orientation measurement precision of 5° with 3000 photons detected from an SM.

Our imaging models have revealed a surprising fundamental limit [25] for measuring accurately the rotational dynamics of SMs. We expect an unconstrained, uniformly rotating dipole emitter to absorb varying input polarizations of light uniformly, to emit uniformly across all possible detection polarizations, and to emit an isotropic angular (energy) spectrum. However, any practical measurement will capture a finite number of photons from the dipole emitter, yielding a finite signal to noise ratio (SNR), and therefore, this expected symmetry is routinely broken. Detailed modelling of the imaging process, including photon shot noise, shows that

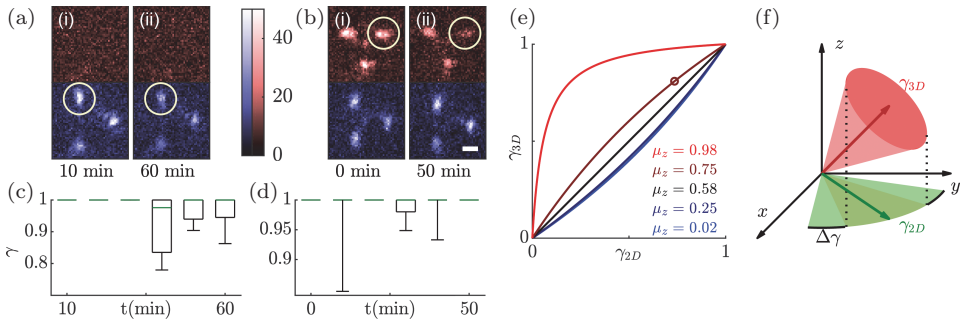

Fig. 1. (colour) Measuring orientation dynamics of single molecules. (a) and (b) Tri-spot images of Atto 647N molecules (a) 1 and (b) 2 at the (i) beginning and (ii) end of time-lapse imaging. Both molecules are embedded in a thin polymer film under continuous exposure to humid air. Circles highlight changes in spot brightness. Scale bar: 1 μm. Colour bar: detected photons/pixel. (c) and (d) Effective rotational constraint of molecules (c) 1 and (d) 2 measured over 50 min. Green: median; Box: first and third quartile; Error bars: minima and maxima. (e) The relation between in-plane γ_{2D} and 3D γ_{3D} rotational constraint varies with an SM's average orientation along the z axis μ_z. (f) A dipole emitter with $\mu_z = 0.75$ and $\gamma_{3D} = 0.81$ (cone half-angle of 30°) appears to be more rotationally free in the xy plane ($\gamma_{2D} = 0.73$, wedge half-angle of 38°). Reprinted figures with permission from Refs. [23–25]. Copyright (2018) by AIP Publishing and (2019) by the American Physical Society.

the expected rotational constraint γ measured in 2D for an isotropic emitter is given by $\mathrm{E}(\gamma_{2D}) = (\pi)^{1/2}/\mathrm{SNR}$, where $\gamma = 0$ represents an isotropic emitter and $\gamma = 1$ represents a rotationally fixed dipole. Therefore, measurements will be biased for all but the highest SNRs. To provide physical intuition, the expected bias in measuring rotational constraint is 0.16 for 1000 signal photons and 30 background photons/pixel, corresponding to a cone angle measurement of 77° (instead of the true value of 90°) for uniform rotational diffusion within a hard-edged cone. Therefore, the molecule always appears to be *more constrained* than it actually is, similar to how a non-moving molecule appears to have a non-zero translational diffusion coefficient because of shot noise.

Further modelling also shows that 2D orientation measurements, i.e., those that capture the in (xy)-plane dipole orientation, and 3D orientation measurements actually perceive identical 3D orientational motions differently (Fig. 1(e) and Ref. [25]). Because 2D methods are blind to the out-of-plane component μ_z, one must have prior knowledge of this quantity in order to compute an equivalent 3D rotational constraint. For small μ_z, the difference between 2D and 3D measurements of motion is small, but for a large $\mu_z = 0.98$ (polar angle = 11°), a highly constrained molecule in 3D ($\gamma_{3D} = 0.80$ or a cone half-angle of 30°) appears to be almost completely rotationally free in two dimensions ($\gamma_{2D} = 0.20$ or a wedge half-angle of 75°, Fig. 1(f)). Therefore, one must exercise caution when using 2D methods to infer rotations in 3D space.

My group also develops algorithms for robustly analysing SMLM datasets that contain images of overlapping molecules [27, 28]. Our analyses have found that

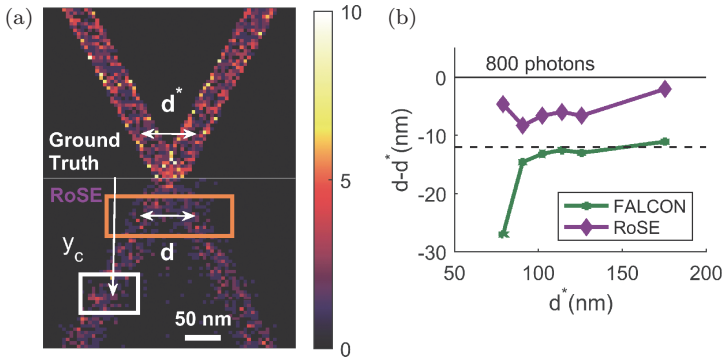

Fig. 2. (colour). Structural bias of two crossing microtubules (MTs) recovered by RoSE [27] (purple) and FALCON. [30] (green). (a) (Top) Simulated ground-truth structure and (bottom) structure obtained by RoSE. (b) Mean separation error between centres of the MTs along the length of the structure for 800 photons detected. Dashed line represents two times the best-possible localization precision given by $(\mathrm{CRB})^{1/2}$. Scale bar: 50 nm. Colour bar: number of localizations per $5 \times 5\,\mathrm{nm}^2$. Adapted with permission from Ref. [27].

localization artefacts tend to not be simply random but instead are structured and correlated with the sample of interest. For example, localizations from overlapping molecules tend to be biased towards their collective centre of mass, making separated microtubules appear closer than they really are and causing circular clusters to appear elliptical. Therefore, scalar error metrics commonly used to evaluate SMLM algorithms, like root mean square error, fail to quantify how the *structure* of the sample itself and the *structure* of the PSF induce systematic *vectorial* artefacts in super-resolved images. Further, these errors are difficult to detect using simple image-based quantities, like the apparent width of the localized PSF or the brightness of the localized molecule. Towards addressing these challenges, we have recently built a methodology, called Wasserstein-induced flux (WIF) [29], to compute the measurement accuracy of any SMLM image without ground truth knowledge of the sample. By measuring computationally the statistical *stability* of each localization within an SMLM reconstruction, WIF can quantify the degree of mismatch between experimental data and a computational model of the imaging system, as well as enhance the accuracy and resolution of SMLM reconstructions. While shot noise makes detecting minor model mismatches difficult, WIF has excellent sensitivity for detecting overlapping molecules and dipole-like emission patterns at SNRs typical of SMLM.

Outlook on Computational Modelling in Fluorescence Nanoscopy

Given the popularity of modern data-driven deep learning and image analysis techniques, one may question the role of traditional physics-based imaging models and statistical models of noise. More fundamentally, why design and build a complicated

imaging system if deep learning can shoulder the burden of creating multi-colour, 3D nanoscope images? First, one must note that photon detection is nonlinear with respect to the photon wave function; cameras are only sensitive to the intensity of light. This nonlinearity destroys some information contained within this wave function, and once this information is lost, no computational algorithm can recover it without using prior knowledge. Therefore, to preserve this information as much as possible, physical optical elements (e.g., lenses, masks, and polarizers) can transform this information into an optimized (intensity) PSF to yield superior measurements. Recent innovations that leverage physical interactions of light with the sample, like MINFLUX [2], DONALD [31], and spectrally resolved SMLM [32–34], show that powerful observations can be made using relatively simple models and imaging algorithms. Second, when executing an imaging task, deep learning algorithms by design impose strong prior knowledge learned during the training process. In most cases, this functionality is useful because it excludes unlikely outcomes, but for scientific imaging, such biases could hinder scientific discovery and lead to erroneous interpretations of an experiment. There exists a need to adopt deep learning architectures whose inner workings are interpretable, so that failure modes for edge cases can be predictable and so that the confidence or trustworthiness of their outputs can be quantified on a *per-experiment* basis. Our work on WIF [29], in which we compute the trustworthiness of each individual localization within a SMLM dataset, is one step towards this goal.

Computational models have the potential to bridge the gap between the chemical and physical processes within living systems and the experimental images produced by fluorescence nanoscopy. Imaging is uniquely suited for revealing the inner workings of these systems because of its ability to correlate dynamic events across space and time by producing rich, high-dimensional datasets. However, end-to-end multiphysics modelling from the target of interest to the measurement (e.g., modelling molecular dynamics within a solvent, interactions of a biomolecule with neighbouring macromolecules, environmental effects on the electronic states of fluorophores, and electromagnetic wave propagation through tissues) is challenging because of the complex physical processes, timescales, and size scales involved. The next frontier is to develop multi-scale techniques that integrate first-principle models and data-driven methods to express how information about an object manifests itself in the measurement domain. Such models will be pivotal for maximizing information transfer from object to measurement and for building imaging systems that directly quantify biochemical dynamics and mechanisms within living systems. These models could bring a paradigm shift in the use of imaging technologies like fluorescence nanoscopy. Instead of considering fluorescent labelling, imaging, and data analysis as separate steps in a protocol, a unified computational model could optimize the entire pipeline simultaneously, thereby maximizing and quantifying statistical certainty on the specific phenomena of interest given the observations in an experiment. Such an intelligent imaging system is yet to come.

Acknowledgments

Hesam Mazidi and Oumeng Zhang made pivotal contributions to the findings discussed in this work with assistance from Jin Lu, Tianben Ding, and Eshan King. Research reported in this publication was supported by the National Science Foundation under grant number ECCS-1653777 and by the National Institute of General Medical Sciences of the National Institutes of Health under grant number R35GM124858.

References

[1] S.W. Hell, *Angew. Chemie Int. Ed.* **54**, 8054 (2015).
[2] F. Balzarotti, Y. Eilers, K.C. Gwosch, A.H. Gynnå, V. Westphal *et al.*, *Science* **355**, 606 (2017).
[3] M.G.L. Gustafsson, *Proc. Natl. Acad. Sci.* **102**, 13081 (2005).
[4] C.B. Müller and J. Enderlein, *Phys. Rev. Lett.* **104**, 198101 (2010).
[5] E. Betzig, *Angew. Chemie Int. Ed.* **54**, 8034 (2015).
[6] W.E. Moerner, *Angew. Chemie Int. Ed.* **54**, 8067 (2015).
[7] J.N. Mait, G.W. Euliss, and R.A. Athale, *Adv. Opt. Photon.* **10**, 409 (2018).
[8] R.J. Ober, S. Ram, and E.S. Ward, *Biophys. J.* **86**, 1185 (2004).
[9] S. Ram, P. Prabhat, J. Chao, E.S. Ward, and R.J. Ober, *Biophys. J.* **95**, 6025 (2008).
[10] M. Badieirostami, M.D. Lew, M.A. Thompson, and W.E. Moerner, *Appl. Phys. Lett.* **97**, 161103 (2010).
[11] M.A. Thompson, M.D. Lew, M. Badieirostami, and W.E. Moerner, *Nano Lett.* **10**, 211 (2010).
[12] H. Deschout, F.C. Zanacchi, M. Mlodzianoski, A. Diaspro, J. Bewersdorf *et al.*, *Nat. Meth.* **11**, 253 (2014).
[13] A. Small and S. Stahlheber, *Nat. Meth.* **11**, 267 (2014).
[14] A. Greengard, Y.Y. Schechner, and R. Piestun, *Opt. Lett.* **31**, 181 (2006).
[15] S.R.P. Pavani, M.A. Thompson, J.S. Biteen, S.J. Lord, N. Liu *et al.*, *Proc. Natl. Acad. Sci.* **106**, 2995 (2009).
[16] Y. Shechtman, S.J. Sahl, A.S. Backer, and W.E. Moerner, *Phys. Rev. Lett.* **113**, 133902 (2014).
[17] A. Von Diezmann, Y. Shechtman, and W.E. Moerner, *Chem. Rev.* **117**, 7244 (2017).
[18] J. Chao, E. Sally Ward, and R.J. Ober, *J. Opt. Soc. Am. A* **33**, B36 (2016).
[19] V.I. Morgenshtern and E.J. Candès, *SIAM J. Imaging Sci.* **9**, 412 (2016).
[20] Y. Shechtman, L.E. Weiss, A.S. Backer, S.J. Sahl, and W.E. Moerner, *Nano Lett.* **15**, 4194 (2015).
[21] T. Kim, S. Moon, and K. Xu, *Nat. Commun.* **10**, 1996 (2019).
[22] E. Hershko, L.E. Weiss, T. Michaeli, and Y. Shechtman, *Opt. Exp.* **27**, 6158 (2019).
[23] O. Zhang, J. Lu, T. Ding, and M.D. Lew, *Appl. Phys. Lett.* **113**, 031103 (2018).
[24] O. Zhang, J. Lu, T. Ding, and M.D. Lew, *Appl. Phys. Lett.* **115**, 069901 (2019).
[25] O. Zhang and M.D. Lew, *Phys. Rev. Lett.* **122**, 198301 (2019).
[26] K. Spehar, T. Ding, Y. Sun, N. Kedia, J. Lu *et al.*, *ChemBioChem* **19**, 1944 (2018).
[27] H. Mazidi, J. Lu, A. Nehorai, and M.D. Lew, *Sci. Rep.* **8**, 13133 (2018).
[28] H. Mazidi, E.S. King, O. Zhang, A. Nehorai, and M.D. Lew, in *2019 IEEE 16th Int. Symp. Biomed. Imaging (ISBI 2019)* (IEEE, 2019), pp. 325–329.
[29] H. Mazidi, T. Ding, A. Nehorai, and M.D. Lew, BioRxiv 721837 (2019).
[30] J. Min, C. Vonesch, H. Kirshner, L. Carlini, N. Olivier *et al.*, *Sci. Rep.* **4**, 4577 (2015).

[31] N. Bourg, C. Mayet, G. Dupuis, T. Barroca, P. Bon *et al.*, *Nat. Photon.* **9**, 587 (2015).
[32] Z. Zhang, S.J. Kenny, M. Hauser, W. Li, and K. Xu, *Nat. Meth.* **12**, 935 (2015).
[33] M.N. Bongiovanni, J. Godet, M.H. Horrocks, L. Tosatto, A.R. Carr *et al.*, *Nat. Commun.* **7**, 13544 (2016).
[34] S. Moon, R. Yan, S. J. Kenny, Y. Shyu, L. Xiang *et al.*, *J. Am. Chem. Soc.* **139**, 10944 (2017).